PAPER

Selective metal ion recognition *via* positional isomers: fluorescent chalcone-1,2,3-triazole hybrids for Co(II) and Cu(II) detection†

Riddima Singh, [ID] [a] Gurleen Singh, [ID] [a] Nancy George,[b] Gurjaspreet Singh,[c] Pallavi Markan,[c] Harminder Singh, [ID] [a] Gurpreet Kaur*[d] and Jandeep Singh [ID] *[a]

This study reports the synthesis of three positional isomers (**6a–6c**) of chalcone-tethered 1,2,3-triazoles *via* the Cu(I)-catalyzed alkyne–azide cycloaddition (CuAAC) reaction. The synthesized probes were comprehensively characterized using FTIR, ^{1}H and ^{13}C NMR, and mass spectrometry. Their potential as metal ion sensors was evaluated through UV-vis and fluorescence spectroscopy, revealing high selectivity and sensitivity toward Co(II) and Cu(II) ions. The probes **6a–c** exhibited low limits of detection (LoD): 1.64 μM (Co(II)) and 3.19 μM (Cu(II)) for ortho isomer (**6a**), 2.08 μM (Co(II)) and 2.30 μM (Cu(II)) for meta substituted (**6b**), and 1.81 μM (Co(II)) and 1.17 μM (Cu(II)) for para-substituted (**6c**) 1,2,3-triazole derivatives. Job's plot analysis confirmed a 1 : 1 metal–ligand complex formation. To further elucidate binding interactions, Density Functional Theory (DFT) calculations were conducted, employing B3LYP/6-31G+(d,p) for free probes and B3LYP/LANL2DZ for their metal complexes. The combined experimental and theoretical results establish a robust and selective sensing platform for Cu(II) and Co(II) detection, with promising applications in environmental monitoring and analytical chemistry.

1. Introduction

The pervasive integration of heavy metals in contemporary industries, coupled with cutting-edge technological advancements, has introduced profound risks that threaten both humans and the environment.[1–3] Notably, cobalt, although necessary in small quantities for the production of vitamin B12 and many enzymatic reactions, can also be very poisonous when present in excessive amounts.[4] Exposure to cobalt in the workplace, which is often found in mining, alloy production, and battery manufacturing sectors, may result in significant health problems. Prolonged exposure to elevated amounts of cobalt may lead to respiratory issues, such as asthma and interstitial lung disease, also known as "hard lung disease." Cobalt poisoning may lead to cardiomyopathy, thyroid dysfunction, and neurological symptoms including hearing loss and vision abnormalities. Consuming food or water contaminated with cobalt may result in systemic toxicity.[5,6]

aSchool of Chemical Engineering and Physical Sciences, Lovely Professional University, Phagwara–144411, Punjab, India. E-mail: singhjandeep@gmail.com

bDivision of Research and Development, Lovely Professional University, Phagwara– 144411, Punjab, India

cDepartment of Chemistry and Centre of Advanced Studies in Chemistry, Panjab University, Chandigarh–160014, India

dDepartment of Chemistry, Gujranwala Guru Nanak Khalsa College, Civil lines, Ludhiana–141001, Punjab, India

† Electronic supplementary information (ESI) available. See DOI: https://doi.org/10.1039/d5ra02187a

Copper plays a crucial role in several biological processes, such as serving as a cofactor for enzymes engaged in redox reactions, facilitating the creation of connective tissue, and aiding in the manufacture of neurotransmitters.[7,8] Excessive buildup of copper may result in hazardous consequences because it can produce reactive oxygen species *via* Fenton-like processes, leading to oxidative stress and harm to cells.[9,10] Prolonged exposure to elevated quantities of copper may lead to severe health issues, including Wilson's disease.[11] Moreover, the occurrence of acute copper poisoning may result in gastrointestinal discomfort, destruction of red blood cells, renal failure, and potentially fatal consequences.[12] Copper pollution resulting from industrial operations, mining, and agricultural runoff may have detrimental effects on aquatic organisms and lead to water resource contamination in the environmental context,[13] highlighting the need for rigorous monitoring and control methods to avoid excessive exposure.[14,15]

Due to the substantial health and environmental hazards linked to copper and cobalt toxicity, it is crucial to create dependable, sensitive, and specific detection techniques. Traditionally, atomic fluorescence spectrometry (AFS),[16] inductively coupled plasma mass spectroscopy (ICP-MS),[17] atomic absorption spectrometry (AAS), electrochemical method, and X-ray absorption spectroscopic techniques were utilized to determine the trace number of heavy metals, are costly, time-consuming, and complex to handle.[18] Consequently, alternative detection strategies like electrochemistry, spectrophotometry, chemosensors, and biosensors are being explored.[19]

Fluorescent sensors are known for their high sensitivity, fast response, and flexibility to detect changes in fluorescence upon interaction with the analytes.[20] Various materials like carbon quantum dots, metal organic frameworks, nanocomposites,[21] inorganic microarchitectures,[22] dyes, polymers, and other organic compounds have been developed as fluorescent sensors for the detection of various pollutants involving cations and anions.[23,24]

Click chemistry is a pivotal method in chemical synthesis known for its rapid and high-yield production of compounds. One of its most prominent techniques is the Copper(I)-catalyzed Azide–Alkyne Cycloaddition (CuAAC), which is a leading method for synthesizing 1,2,3-triazoles via the cyclization of an azide and an alkyne.[25,26] By designing triazole-based ligands, sensors can be customized to detect specific metal ions with high sensitivity and selectivity.[27] The coordination abilities of the 1,2,3-triazole moiety allow it to interact selectively with metal ions, resulting in noticeable changes in photophysical properties, and has been utilized to detect metal ions such as copper, cobalt, lead, mercury, and zinc, etc. in various environmental, biomedical, and analytical contexts.[28,29] The use of 1,2,3-triazoles as selective chemosensors highlights their importance in creating functional materials for ion detection, advancing both chemical synthesis and analytical science.

In this study, novel positional isomeric chalcone-based 1,2,3-triazole derivatives were synthesized via 'CuAAC' methodology and characterized utilizing various spectroscopic techniques including IR, NMR (^{1}H and ^{13}C), and mass spectrometry. The sensing behavior of the probes was elucidated via UV-visible and fluorescence spectroscopy for the detection of Co(II) and Cu(II) ions. Furthermore, density functional theory (DFT) calculations, were applied successfully to probes to obtain detailed structural and electronic insights of the sensor and its interactions with metal ions. Despite the variation in the position of the benzoyl unit, probes **6a–6c**, which correspond to the ortho, meta, and para isomers, exhibit consistent sensing capabilities toward the target metal ions. Interestingly, this positional change does not significantly affect their ability to interact with the analytes. This consistency can be attributed to their overall molecular framework and the presence of a common binding cavity formed by the nitrogen atoms of the 1,2,3-triazole ring, which enables effective coordination with the target metal ions. However, noticeable variations are observed in key sensing parameters such as the limit of detection (LOD), limit of quantification (LOQ), and binding constant values, indicating that while the fundamental sensing mechanism remains intact, the binding efficiency is influenced by the specific isomeric arrangement.

2. Experiment

Caution! sodium azide is sensitive to heat & shock and should be handled with extreme care.

2.1. Materials and method

All the experimental work was performed under standard laboratory conditions using following starting materials: 4-chlorobenzaldehyde, 2-aminoacetophenone, 3-aminoacetophenone, 4-aminoacetophenone supplied from LOBA, propargyl bromide solution (80% by weight in toluene) (spectrochem), N, N-dimethylformide (DMF) (LOBA), potassium carbonate (LOBA), tetrahydrofuran (LOBA), triethylamine (LOBA), and bromotris(triphenylphosphine)copper(I) [CuBr(PPh$_3$)$_3$] (Aldrich). The synthesized compounds were characterized using various spectroscopic techniques. Infrared (IR) spectra were recorded neat on the SHIMADZU FTIR-8400S spectrometer. NMR spectra, including ^{1}H and ^{13}C NMR, were acquired on a Bruker Advance Neo FT NMR spectrometer using CDCl$_3$ as the solvent and tetramethylsilane (TMS) as the internal standard for chemical shift referencing. Mass spectra (LCMS) were obtained with a Waters Micromass Q-Tof Micro mass spectrometer. Melting points were determined using a Mel Temp II instrument and were uncorrected. Elemental analyses (CHN) were conducted with a PerkinElmer Model 2400 CHNS element analyzer. UV-visible absorption and fluorescence studies were performed using a quartz cuvette on a SHIMADZU UV-1900 spectrometer and a PerkinElmer 6500 fluorescence spectrophotometer, respectively. Computational analysis was carried out using density functional theory (DFT) with the Gaussian software package.

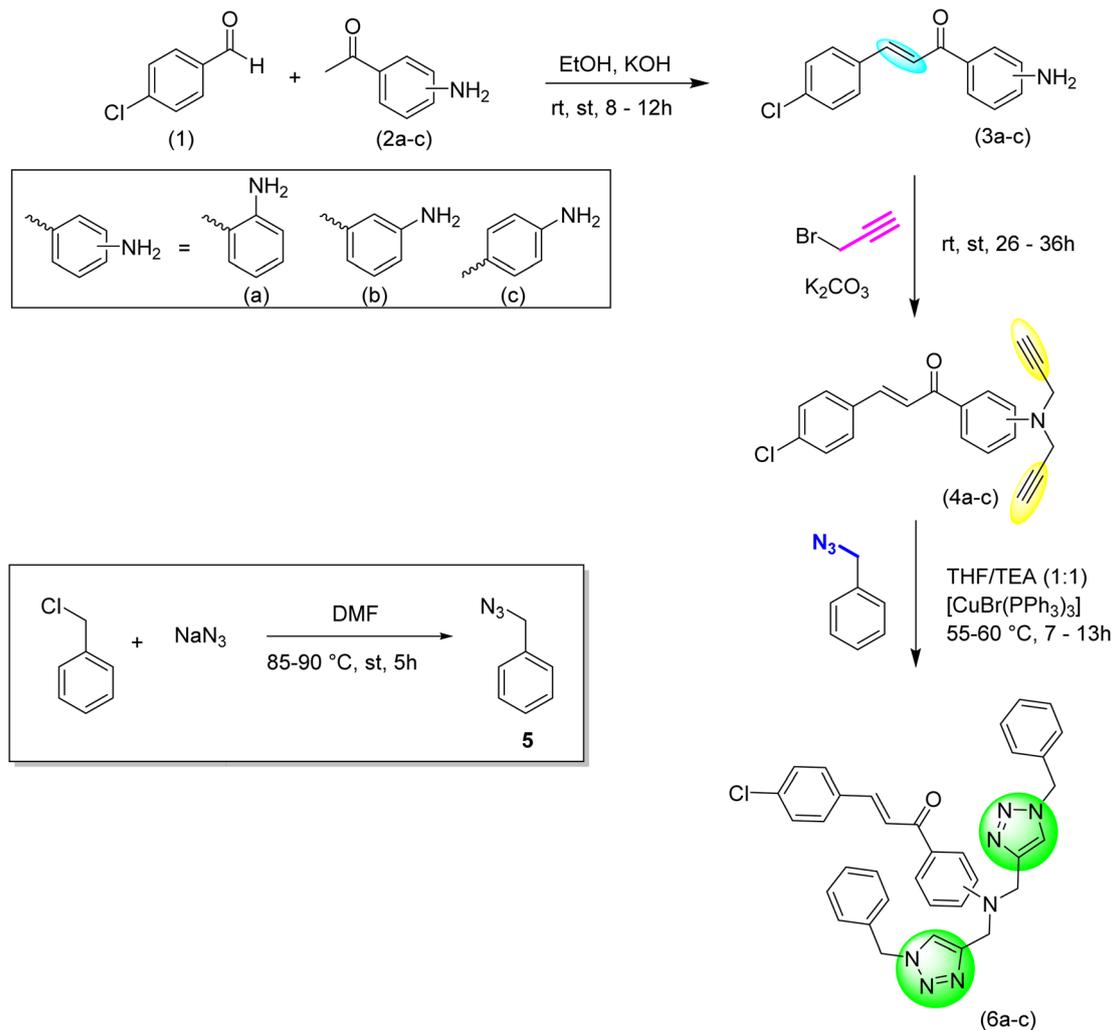### 2.2. Synthesis and characterization of chalcones (3a–3c)

The initial reactants were dissolved in ethanol while being stirred continuously. Potassium hydroxide was then slowly added to this mixture (Scheme 1). The mixture was stirred at room temperature until the reactants were completely converted into the desired products, with the progress tracked using TLC (ethyl acetate: hexane, 1:9). To quench the reaction, ice-cold water was added to the mixture, which was then filtered and the solid product was dried. The final product was purified using ethanol as the eluent.[30]

2.2.1. (E)-1-(2-aminophenyl)-3-(4-chlorophenyl)prop-2-en-1-one (3a). The above-mentioned procedure was followed for the synthesis process. The quantities used were: 4-chlorobenzaldehyde (2 g, 14.22 mmol), 2-aminoacetophenone (1.72 mL, 14.22 mmol), potassium hydroxide (5 mL, 20% w/v). Yield: 90%; colour: yellow; texture: solid powder; M.F. = C$_{15}$H$_{12}$ClNO; elem. anal. calc. (%): C = 69.91; H = 4.69, N = 5.44; found (%): C = 69.87, H = 4.71, N = 5.42; Mp.: 92–93 °C, IR (neat, cm^{-1}): 3461, 3295, 3032, 1639, 1606, 1564, 1533, 1484, 1404, 1328, 1280, 1207, 1154, 1083, 994, 822, 747.

2.2.2. (E)-1-(3-aminophenyl)-3-(4-chlorophenyl)prop-2-en-1-one (3b). The above-mentioned procedure was followed for the synthesis process. The quantities used were: 4-chlorobenzaldehyde (0.5 g, 3.55 mmol), 2-aminoacetophenone (0.47 g, 3.55 mmol), and potassium hydroxide (5 mL, 20% w/v). Yield: 92%; colour: yellow; texture: solid powder; M.F. = C$_{15}$H$_{12}$ClNO; elem. anal. calc. (%): C = 69.91; H = 4.69, N = 5.44; found (%): C = 69.87, H = 4.71, N = 5.42; Mp.: 98–99 °C, IR (neat, cm^{-1}): 3449, 3359, 3047, 2868, 1658, 1585, 1487, 1441, 1317, 1215, 1160, 1087, 978, 911, 824, 783, 681, 631.

2.2.3. (E)-1-(4-aminophenyl)-3-(4-chlorophenyl)prop-2-en-1-one (3c). The above-mentioned procedure was followed for the synthesis process. The quantities used were: 4-

Scheme 1 Schematic representation of the synthesis of ortho, meta, and para-substituted chalcones, their corresponding alkynes and 1,2,3-triazoles.

chlorobenzaldehyde (0.5 g, 3.55 mmol), 2-aminoacetophenone (0.47 g, 3.55 mmol), and potassium hydroxide (5 mL, 20% w/v). Yield: 87%; colour: yellow; texture: solid powder; M.F. = $C_{15}H_{12}ClNO$; elem. anal. calc. (%): C = 69.91, H = 4.69, N = 5.44; found (%): C = 69.87, H = 4.71, N = 5.42; Mp.: 135–136 °C, IR (neat, cm^{-1}): 3457, 3340, 3054, 1635, 1598, 1541, 1490, 1446, 1343, 1224, 1172, 1087, 1017, 980, 811, 672, 597.

2.3. Synthesis and characterization of chalcone-based alkynes (4a–4c)

The chalcone was dissolved in DMF with constant stirring, then anhydrous potassium carbonate was introduced, followed by the gradual, dropwise addition of propargyl bromide. The reaction mixture was stirred at ambient temperature and monitored *via* TLC using a mixture of ethyl acetate and hexane. After quenching the reaction with ice-cold water, the resulting solid product was filtered and air-dried at room temperature.

2.3.1. (E)-3-(4-chlorophenyl)-1-(2-(di(prop-2-yn-1-yl)amino) phenyl)prop-2-en-1-one (4a). The above-mentioned procedure

was followed for the synthesis process. The quantities used were as follows: ortho-substituted chalcone (1.0 g, 3.88 mmol), anhydrous potassium carbonate (2.68 g, 19.4 mmol), propargyl bromide (1.06 mL, 9.3 mmol), DMF (20 mL). Yield: 93%; colour: yellow; texture: solid powder; M.F. = $C_{21}H_{16}ClNO$; elem. anal. calc. (%): C = 75.56, H = 4.83, N = 4.20; found (%): C = 75.54, H = 4.82, N = 4.18; IR (neat, cm^{-1}): 3279, 3069, 2925, 2862, 2113, 1640, 1574, 1497, 1411, 1278, 1202, 1153, 1079, 999, 818, 742, 636; ^{1}H NMR (500 MHz, CDCl$_3$): δ = 7.91 (d, J = 7.5 Hz, 1H), 7.83 (s, 1H), 7.65–7.54 (m, 3H), 7.46 (d, J = 8.0 Hz, 1H), 7.37 (d, J = 8.4 Hz, 2H), 6.87 (s, 2H), 4.07 (s, 4H), 2.25 (s, 2H); ^{13}C NMR (126 MHz, CDCl$_3$): δ = 191.72, 168.11, 150.84, 141.75, 136.21, 135.36, 134.73, 134.01, 131.85, 131.17, 129.68, 129.43, 123.81, 80.45, 71.64, 38.98.

2.3.2. (E)-3-(4-chlorophenyl)-1-(3-(di(prop-2-yn-1-yl)amino) phenyl)prop-2-en-1-one (4b). The above-mentioned procedure was followed for the synthesis process. The quantities used were as follows: meta-substituted chalcone (1.0 g, 3.88 mmol), anhydrous potassium carbonate (2.68 g, 19.4 mmol), propargyl bromide (1.06 mL, 9.3 mmol), DMF (20 mL). Yield: 90%; colour:

yellow; texture: solid powder; M.F. = $C_{21}H_{16}ClNO$; elem. anal. calc. (%): C = 75.56, H = 4.83, N = 4.20; found (%): C = 75.57, H = 4.84, N = 4.19; IR (neat, cm^{-1}): 3289, 3065, 2938, 2112, 1671, 1587, 1488, 1439, 1326, 1261, 1090, 983, 912, 823, 782, 642; ^{1}H NMR (500 MHz, CDCl$_3$): δ = 7.81 (d, J = 8.3 Hz, 1H), 7.73 (d, J = 15.7 Hz, 2H), 7.62–7.52 (m, 2H), 7.51–7.35 (m, 3H), 7.18 (d, J = 8.3 Hz, 2H), 4.18 (s, 4H), 2.28 (s, 2H); ^{13}C NMR (126 MHz, CDCl$_3$): δ = 190.51, 147.96, 143.20, 138.91, 136.34, 133.42, 130.89, 130.11, 129.55, 129.37, 129.21, 122.79, 115.02, 78.76, 73.03, 40.48.

2.3.3. (E)-3-(4-chlorophenyl)-1-(4-(di(prop-2-yn-1-yl)amino)phenyl)prop-2-en-1-one (4c).

The above-mentioned procedure was followed for the synthesis process. The quantities used were as follows: para-substituted chalcone (1.0 g, 3.88 mmol), anhydrous potassium carbonate (2.68 g, 19.4 mmol), propargyl bromide (1.06 mL, 9.3 mmol), DMF (20 mL). Yield: 89%; colour: yellow; texture: solid powder; M.F. = $C_{21}H_{16}ClNO$; elem. anal. calc. (%): C = 75.56, H = 4.83, N = 4.20; found (%): C = 75.55, H = 4.82, N = 4.22; IR (neat, cm^{-1}): 3324, 3067, 2929, 2116, 1656, 1594, 1486, 1407, 1332, 1275, 1225, 1176, 1079, 1019, 975, 811, 743, 663; ^{1}H NMR (500 MHz, CDCl$_3$): δ = 7.98 (d, J = 18.5 Hz, 2H), 7.62 (d, J = 87.2 Hz, 3H), 7.32 (d, J = 42.9 Hz, 3H), 6.94 (s, 2H), 4.11 (d, J = 106.8 Hz, 4H), 2.27 (s, 2H); ^{13}C NMR (126 MHz, CDCl$_3$): δ = 187.76, 167.79, 151.04, 141.58, 130.95, 129.42, 129.12, 128.80, 128.16, 122.47, 112.35, 79.83, 68.17, 38.72.

2.4. Synthesis of organic azide

A solution of benzyl chloride (5.5 g, 47.8 mmol) in 25 mL of DMF was prepared using a magnetic stirrer, and sodium azide (15.5 g, 239 mmol) was then added. The reaction mixture was heated to 85–90 °C and refluxed for 5 hours, with completion confirmed by TLC analysis using a 1 : 4 mixture of ethyl acetate and hexane. The product was extracted using ethyl acetate, and the combined organic layers were dried with anhydrous sodium sulfate, filtered, and subjected to vacuum evaporation to remove the remaining solvent.[23] Yield = 60%; color: light yellow; texture = oil; M.F.: $C_7H_7N_3$; IR (neat, cm^{-1}): 3032, 2930, 2089, 1452, 1252, 876, 697, 568; ^{1}H NMR (500 MHz, CDCl$_3$) δ = 7.27–7.12 (m, 5H), 4.14 (s, 2H) ppm; ^{13}C NMR (126 MHz, CDCl$_3$) δ = 135.53, 128.91, 128.37, 128.31, 54.82 ppm.

2.5. Synthesis and characterization of 1,2,3-triazoles (6a–6c)

The chalcone-based terminal alkyne was dissolved in a THF/TEA solvent system, to which the organic azide was subsequently added, followed by the Cu(ɪ) catalyst. The reaction mixture was refluxed at 55–60 °C until the reactants were completely converted, as verified by TLC (ethyl acetate: hexane, 1 : 4). The reaction was quenched by adding ice-cold water. If the resulting product was solid, it was filtered, washed with distilled water, and allowed to air-dry at room temperature. For liquid products, solvent extraction was conducted using ethyl acetate. The combined organic phases were dried over anhydrous sodium sulfate, and the solvent was evaporated under vacuum to obtain the pure product.

2.5.1. (E)-1-(2-(bis((1-benzyl-1H-1,2,3-triazol-4-yl)methyl)amino)phenyl)-3-(4-chlorophenyl)prop-2-en-1-one (6a).

The above-mentioned procedure was followed for the synthesis process. The quantities used were as follows: ortho-substituted chalcone-based alkyne (0.70 g, 1.72 mmol), benzyl azide (0.43 mL, 3.46 mmol), Cu(ɪ) catalyst (0.001 mmol), THF/TEA (1 : 1) (8 mL). Yield: 92%; colour/texture: yellow powder; M.F.: $C_{35}H_{30}ClN_7O$; elem. anal. calc. (%): C = 75.56, H = 4.83, N = 4.20; found (%): C = 75.55, H = 4.82, N = 4.22; mp: 127–128 °C; IR (neat, cm^{-1}): 3071, 2953, 2851, 1642, 1573, 1505, 1413, 1301, 1260, 1200, 1162, 1088, 1046, 1013, 972, 810, 749, 712, 635, 573. ; ^{1}H NMR (500 MHz, CDCl$_3$): δ = 7.88 (d, J = 7.8 Hz, 1H), 7.62 (d, J = 7.6 Hz, 2H), 7.53 (d, J = 8.3 Hz, 3H), 7.37–7.31 (m, 9H), 7.23 (d, J = 6.2 Hz, 3H), 6.80 (d, J = 8.1 Hz, 2H), 6.67 (t, J = 7.5 Hz, 2H), 5.48 (s, 4H), 4.60 (s, 4H).; ^{13}C NMR (126 MHz, CDCl$_3$): δ = 191.39, 151.24, 141.34, 135.94, 135.22, 134.62, 133.76, 131.57, 129.38, 129.16, 129.09, 128.71, 127.97, 123.57, 114.99, 112.23, 54.22, 39.05.; LC-MS: m/z (calculated) = 599.22; m/z (found) = 600.12 (M+1).

2.5.2. (E)-1-(3-(bis((1-benzyl-1H-1,2,3-triazol-4-yl)methyl)amino)phenyl)-3-(4-chlorophenyl)prop-2-en-1-one (6b).

The above-mentioned procedure was followed for the synthesis process. The quantities used were as follows: meta-substituted chalcone-based alkyne (0.70 g, 1.72 mmol), benzyl azide (0.43 mL, 3.46 mmol), Cu(ɪ) catalyst (0.001 mmol), THF/TEA (1 : 1) (8 mL). Yield: 86%; Colour/texture: brown viscous oil; M.F.: $C_{35}H_{30}ClN_7O$; IR (neat, cm^{-1}): 3139, 3060, 2963, 1671, 1590, 1487, 1447, 1327, 1260, 1090, 1016, 798, 700, 540; ^{1}H NMR (500 MHz, CDCl$_3$): δ = 7.70 (d, J = 15.7 Hz, 1H), 7.62–7.54 (m, 2H), 7.54–7.47 (m, 1H), 7.47–7.40 (m, 2H), 7.40–7.34 (m, 6H), 7.25–7.21 (m, 1H), 7.21–7.18 (m, 2H), 7.18–7.12 (m, 6H), 7.10–7.02 (m, 1H), 5.42–5.35 (m, 4H), 4.68 (d, J = 12.6 Hz, 4H); ^{13}C NMR (126 MHz, CDCl$_3$): δ = 189.48, 147.11, 141.92, 137.86, 133.68, 133.61, 129.88, 128.66, 128.19, 127.97, 127.65, 126.77, 125.79, 121.77, 121.21, 117.21, 116.89, 115.80, 112.23, 111.57, 53.06, 45.68; LC-MS: m/z (calculated) = 599.21; m/z (found) = 600.22 (M+1).

2.5.3. (E)-1-(4-(bis((1-benzyl-1H-1,2,3-triazol-4-yl)methyl)amino)phenyl)-3-(4-chlorophenyl)prop-2-en-1-one (6c).

The above-mentioned procedure was followed for the synthesis process. The quantities used were as follows: para-substituted chalcone-based alkyne (0.70 g, 1.72 mmol), benzyl azide (0.43 mL, 3.46 mmol), Cu(ɪ) catalyst (0.001 mmol), THF/TEA (1 : 1) (8 mL); yield: 88%; colour/texture: brown viscous oil; M.F.: $C_{35}H_{30}ClN_7O$; IR (neat, cm^{-1}): 3047, 2926, 1654, 1587, 1509, 1323, 1228, 1168, 1018, 814, 736, 684; ^{1}H NMR (500 MHz, CDCl$_3$): δ = 7.95 (s, 1H), 7.73 (d, J = 13.5 Hz, 3H), 7.63 (s, 1H), 7.45 (d, J = 9.3 Hz, 8H), 7.37 (d, J = 11.7 Hz, 7H), 6.95 (s, 2H), 5.46 (s, 4H), 4.22 (s, 4H); ^{13}C NMR (126 MHz, CDCl$_3$): δ = 187.78, 161.13, 141.62, 133.83, 130.96, 130.21, 129.65, 129.42, 129.14, 128.86, 127.70, 127.49, 121.89, 113.93, 112.36, 68.18, 38.73; LC-MS: m/z (calculated) = 599.22; m/z (found) = 600.27 (M+1).

3. Results and discussions

3.1. Synthesis

The synthesis of probes **6a–6c** involves a three-step process, starting with the synthesis of chalcone. First, chalcone is synthesized, followed by its conversion into an alkyne *via*

nucleophilic substitution. Potassium carbonate acts as the catalyst, reacting with the propargyl group and substituting the dynamic protons of the chalcone with propargyl moieties, resulting in a terminal alkyne. In the subsequent step, alkyne and azide are fused, using tetrahydrofuran (THF) as the solvent, triethylamine (TEA) as the base, and [CuBr(PPh$_3$)$_3$] as the catalyst, ultimately forming the desired product.

3.2. Spectroscopic analysis

3.2.1. Infrared (IR) spectroscopy. The IR spectroscopy results for terminal alkynes (**4a–4c**), benzyl azide (**5**), and chalcone-based 1,2,3-triazole derivatives (**6a–6c**) in the range of 4000–500 cm^{-1} were consistent with the predicted values. The IR spectrum of terminal alkyne **4a** exhibited characteristic stretching bands for the C≡C–H and C≡C groups at 3279 cm^{-1} and 2113 cm^{-1}, respectively. Similarly, terminal alkyne **4b** showed peaks at 3289 cm^{-1} and 2112 cm^{-1}, while terminal alkyne **4c** displayed peaks at 3324 cm^{-1} and 2116 cm^{-1}, confirming the successful synthesis of the alkyne derivatives. The IR spectrum of benzyl azide revealed a prominent band at 2089 cm^{-1}, corresponding to the N$_3$ stretching of the azide group. For all cases, the disappearance of absorption bands near 3279–3324 cm^{-1} (C≡C–H stretching), 2112–2116 cm^{-1} (C≡C stretching), and 2089 cm^{-1} (–N=N=N stretching) confirmed the modification of the C≡C–H and N$_3$ groups, thereby verifying the successful synthesis of the 1,2,3-triazole moieties.

3.2.2. NMR spectroscopy and mass spectrometry. The NMR (^{1}H and ^{13}C) analysis provided additional confirmation of the successful synthesis of the terminal alkynes (**4a–4c**) and the 1,2,3-triazole derivatives (**6a–6c**). In the ^{1}H NMR spectra, a singlet at $\delta = 2.25$ ppm was observed for the alkynyl proton (C≡C–H) in alkyne **4a**, while similar singlets were observed at $\delta = 2.28$ ppm for **4b** and $\delta = 2.27$ ppm for **4c**. Supporting these observations, the ^{13}C NMR spectra further confirmed the presence of the C≡C carbons in the terminal alkynes (**4a–c**). For **4a**, signals were observed at $\delta = 71.64$ ppm and $\delta = 80.45$ ppm, corresponding to the sp-hybridized carbons of the alkyne group.

Similarly, the ^{13}C NMR spectrum of **4b** displayed signals at $\delta = 73.03$ ppm and $\delta = 78.76$ ppm, while **4c** exhibited signals at $\delta = 71.93$ ppm and $\delta = 79.84$ ppm, conclusively verifying the successful formation of the terminal alkyne moieties. For all three compounds, the absence of the characteristic triplet at around $\delta = 2.25$–2.28 ppm, which would indicate alkynyl protons in the precursors, confirmed the complete transformation into the 1,2,3-triazole structure. The mass spectra of the 1,2,3-triazole derivatives (**6a–6c**) exhibited molecular ion peaks consistent with the predicted values. For **6a**, the expected molecular mass peak was $m/z = 599.22$, and the observed spectrum showed a prominent [M+1]$^+$ peak at $m/z = 600.12$. Similarly, the mass spectra of **6b** and **6c** revealed strong [M+1]$^+$ peaks at $m/z = 600.22$ and $m/z = 600.27$, respectively, confirming the successful synthesis of the compounds.

3.3. UV-vis analysis to scrutinize the chemosensing behavior of probe 6a–c

The UV-vis spectral investigations designed to assess the chemosensing behavior of probes **6a–6c** produced significant results, confirming their ion recognition potential. Given the solubility of the probes in the THF : H$_2$O (4 : 1) mixture, this solvent system was employed for the UV-vis spectroscopy experiments. Concentrations of 0.02 mM, 0.05 mM, and 0.02 mM for probes **6a–c** respectively were optimized based on their appropriate absorption bands. Probe **6a** exhibited an absorption peak at 311 nm, probe **6b** at 317 nm, and probe **6c** at 362 nm. To determine the sensitivity of the probes to various ions, chlorides of Ba(II), Ca(II), Co(II), Cr(III), Cu(II), Pb(II), Hg(II), Mn(II), Mg(II), Ni(II), Zn(II), Cd(II), Ce(III), Na(I), K(I) were dissolved in THF : H$_2$O (4 : 1) mixture and utilized. Only Co(II) and Cu(II) demonstrated significant shifts in absorbance peaks upon titration with the probe solutions, while other metal ions exhibited no notable change in absorption peaks and intensity. Fig. S28–S30† depicts the relative chemosensing performances of probes **6a–6c** towards various metal ions at equimolar concentrations, underscoring a significantly higher response to Co(II) and Cu(II). Despite the variation in the position of the
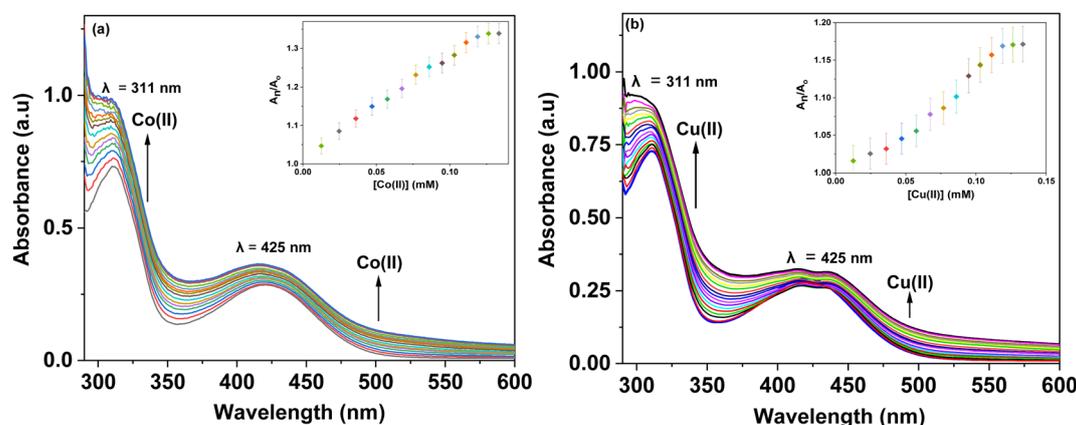

Fig. 1 Shifts in the absorption maxima of probe **6a** observed during titration with (a) Co(II) and (b) Cu(II); the inset exhibits the relative absorbance change of probe **6a** (A_n/A_0) and metal ion concentration (mM).
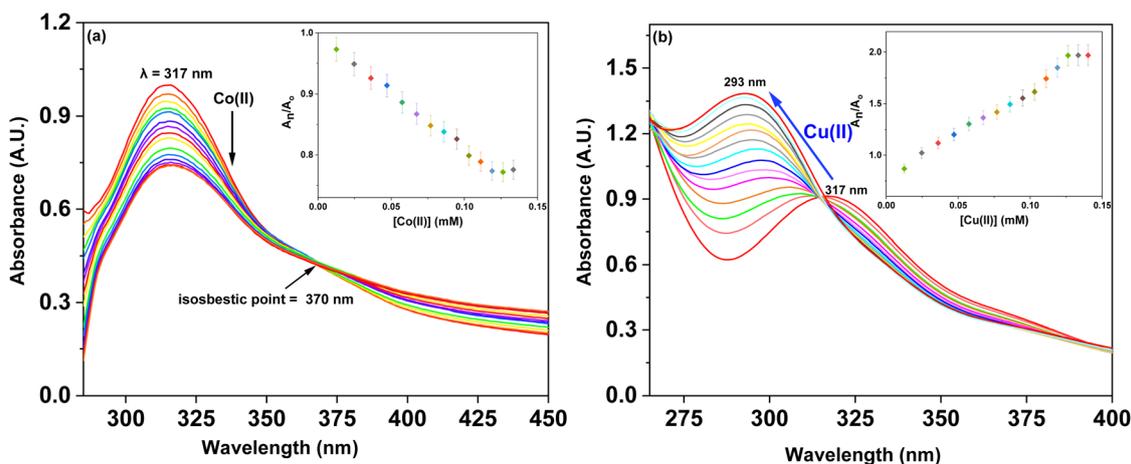
Fig. 2 Shifts in the absorption maxima of probe **6b** observed during titration with (a) Co(II) and (b) Cu(II); the inset exhibits the relative absorbance change of probe (A_n/A_0) and metal ion concentration (mM).

benzoyl unit, probes **6a–6c** consistently demonstrated sensing capabilities towards the target metal ion, indicating that their interaction efficiency with the analyte remains intact. This consistency is attributed to the overall molecular architecture and identical binding cavity of the probes (N atoms of the triazole ring), which facilitates effective interaction with the target species. Nonetheless, there are noticeable differences in the detection limit and binding constant values among the probes.

3.3.1. Response of probes 6a–6c towards Co(II) and Cu(II). The interactions of probes **6a–c** with Co(II) and Cu(II) ions were systematically investigated using UV-vis spectroscopy. In these experiments, solutions of each probe were titrated with 1 mM solutions of Co(II) and Cu(II) ions in separate titrations. For probe **6a**, the addition of Co(II) ions resulted in a significant hyperchromic shift in the absorption peak observed at 311 nm, accompanied by a smaller hyperchromic shift at 425 nm. These changes are attributed to $n \rightarrow \pi^*$ transitions, indicating a strong interaction between the probe and Co(II) ions. Similarly, titration with Cu(II) ions led to pronounced hyperchromic

shifts at 311 nm and minor hyperchromic changes at 425 nm as depicted in Fig. 1a and b. For probe **6b**, on the gradual addition of a 1 mM Co(II) solution to the probe, the absorption peak at 317 nm exhibited a pronounced hypochromic shift, characterized by a decrease in intensity. This shift was accompanied by the emergence of an isosbestic point at 370 nm. In contrast, the incremental addition of a 1 mM Cu(II) solution induced a notable blue shift of approximately 24 nm in the absorption maximum, shifting it from 317 nm to 293 nm. This shift was further accompanied by a significant hyperchromic effect at 293 nm, highlighting an increase in absorbance intensity (Fig. 2a and b).

The stepwise addition of Co(II) ions to the solution of probe **6c** resulted in a pronounced hyperchromic shift in the absorption peak at 362 nm, indicative of $n \rightarrow \pi^*$ transitions. This spectral change was accompanied by the emergence of an isosbestic point at 284 nm. In the case of Cu(II), the incremental addition of a 1 mM Cu(II) solution induced a notable hyperchromic shift at 279 nm accompanied by the formation of an
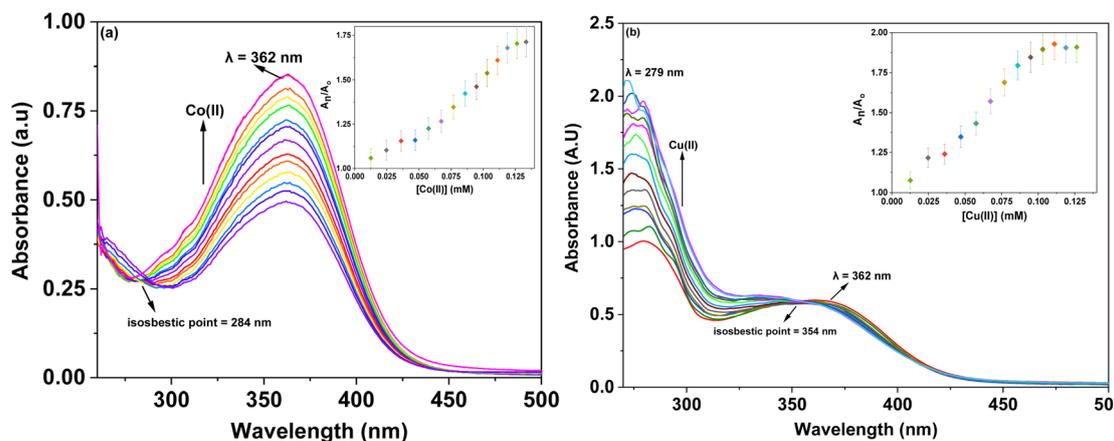

Fig. 3 Shifts in the absorbance peak of probe **6c** observed during titration with (a) Co(II) and (b) Cu(II); the inset exhibits the relative absorbance change of probe (A_n/A_0) and metal ion concentration (mM).
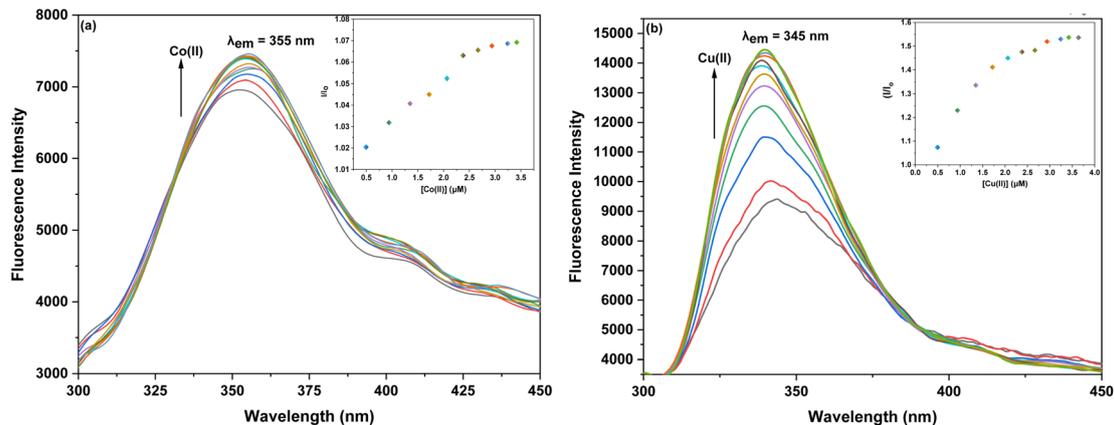
Fig. 4 Variations in the fluorescence emission of probe **6a** upon the incremental addition of (a) Co(II) and (b) Cu(II); the inset illustrates the relative change in emission of probe *versus* metal ion concentration (μM).

isosbestic point 354 nm (Fig. 3a and b). Furthermore, the inset plots in figures, illustrate the relative changes in maximum absorbance (A_n/A_0) for probes **6a–c**, where A_n represents the absorption maxima recorded after successive additions of the metal ions, and A_0 corresponds to the initial absorption maxima of each probe.

Additionally, the association constant (K_a) for the host–guest complexation (1:1) was calculated using the Benesi–Hildebrand eqn (1). The corresponding Benesi–Hildebrand plots for the complexation of probes **6a–c** with Co(II) as well as Cu(II) are presented in Fig. S31–S36.† The K_a values for probe **6a** for Co(II) and Cu(II) ions were 8.80×10^3 M^{-1}, 5.99×10^3 M^{-1}, while those for probes **6b** and **6c** for the aforementioned metal ions were 7.66×10^3 M^{-1}, 4.74×10^3 M^{-1}, and 6.61×10^3 M^{-1}, 1.00×10^4 M^{-1}, respectively. Moreover, the binding ratio of 1:1 (M:L) was established for all three probes based on the Job's plots analysis (graphs are given in ESI, Fig. S49–S54†).

$$\frac{1}{A - A_0} = \frac{1}{A' - A_0} + \frac{1}{K_a \left(A' - A_0 \right) [M^{n+}]} \tag{1}$$

where A_0 = initial absorption intensity, A = absorption intensity with a specific concentration of metal ions, A' = final absorption intensity, $[M^{n+}]$ = concentration of metal ions, and, K_a = association constant.

3.3.2 Time-dependent analysis of probes 6a–6c. The time-dependent behavior of the metal-bound probes **6a–6c** was evaluated to gain insights into their stability and sensitivity toward metal ions. Absorption spectroscopy was employed to monitor the effect of time on these metal-bound probes. As depicted in the corresponding Fig. S37–S42,† the absorbance of Co(II)– and Cu(II)-complexed solutions of probes **6a–c** remained consistent, showing no significant variation even after extended periods of standing. These findings confirm that the probes exhibit excellent stability and maintain a strong, robust affinity for the respective metal ions over time.

3.3.3 Temperature-dependent analysis of probes 6a–6c. The influence of temperature on the binding efficiency of probes **6a–6c** was investigated by recording the absorption spectra of their metal-bound complexes at 2 °C intervals over a temperature range of 20 °C to 50 °C. As illustrated in the accompanying Fig. S43–S48† no significant changes were
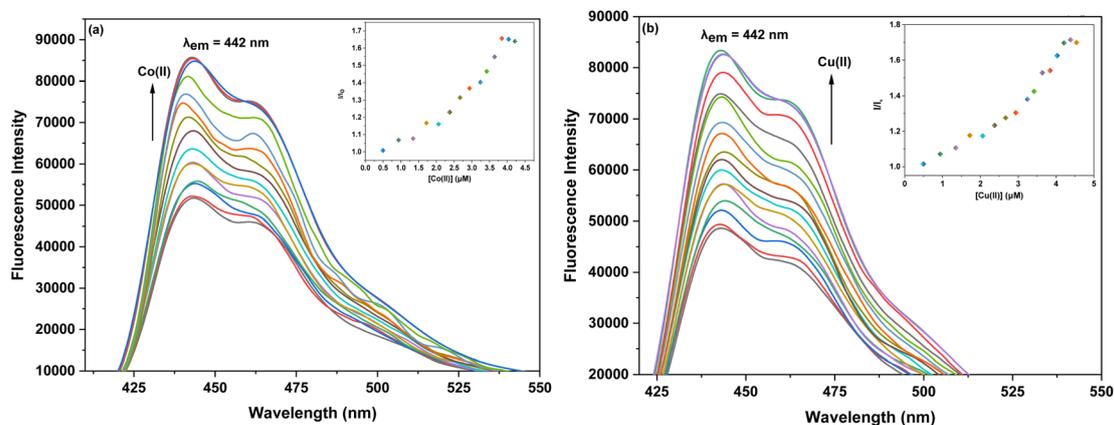

Fig. 5 Variations in the fluorescence emission of probe **6b** upon the incremental addition of (a) Co(II) and (b) Cu(II); the inset illustrates the relative change in emission of probe *versus* metal ion concentration (μM).
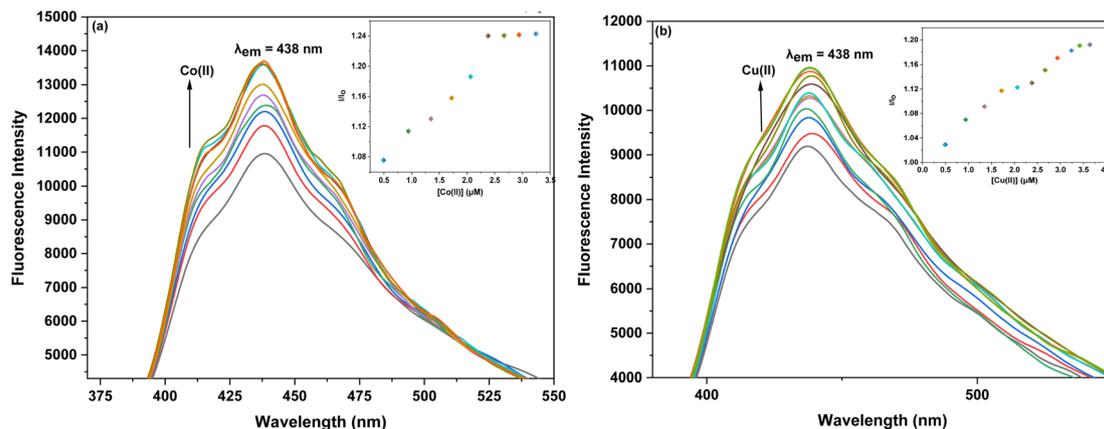
Fig. 6 Changes in the emission of probe **6c** with the gradual addition of (a) Co(II) and (b) Cu(II). The inset shows the relative emission change of the probe as a function of metal ion concentration (μM).

observed in the binding behavior of the probes across the tested temperatures. These results highlight the thermal stability and robustness of the interactions between the probes and the metal ions, demonstrating their consistent performance under varying thermal conditions.

3.3.4 Competitive metal ion titration for probe 6a–6c. The selectivity of probes **6a–6c** was further assessed in the presence of all metal ions simultaneously, prepared in an equimolar ratio. A single solution containing an equimolar mixture of various metal ions was titrated with each probe, and the resulting UV-vis spectra were analyzed (Fig. S55–S57†). It was observed that the spectra obtained during these titrations closely matched those recorded when Co(II) was used alone with the probes. This finding indicates that each probe selectively recognized Co(II) even in the presence of other competing metal ions. These results conclusively demonstrate that all three probes exhibit high selectivity for Co(II), with no interference from other metal ions, thereby confirming their robust chemosensing properties.

3.3.5 Chemosensing behavior of probe 6a–c *via* fluorescence spectroscopy. The interactions of probes **6a–c** with Co(II)

and Cu(II) ions were also examined through fluorescence spectroscopy, where solutions of each probe were titrated with 10 μM solutions of the metal ions in separate experiments. When exposed to an excitation wavelength (λ_{ex}) of 295 nm, probe **6a** exhibited a prominent emission peak (λ_{em}) at 445 nm. Independent titrations for both Co(II) and Cu(II) ions, as shown in Fig. 4a and b demonstrated that the fluorescence emission intensity of probe **6a** increased upon the introduction of either of the metal ions into the solution. The concentration of the probe was maintained at 5 μM throughout the experiment, while the metal ion concentration was progressively increased up to 15 equivalents.

For probe **6b**, upon excitation at a wavelength of (λ_{ex}) 320 nm, a distinct fluorescence emission peak was observed at (λ_{em}) 442 nm. The fluorescence intensity of probe **6b** significantly increased upon the addition of Co(II) and Cu(II) ions, as depicted in the corresponding Fig. 5a and b. During the experiments, the concentration of the probe was maintained consistently at 5 μM, while the concentration of the metal ions was systematically increased in incremental steps, reaching up to 15 equivalents relative to the probe. In the case of probe **6c**, when exposed
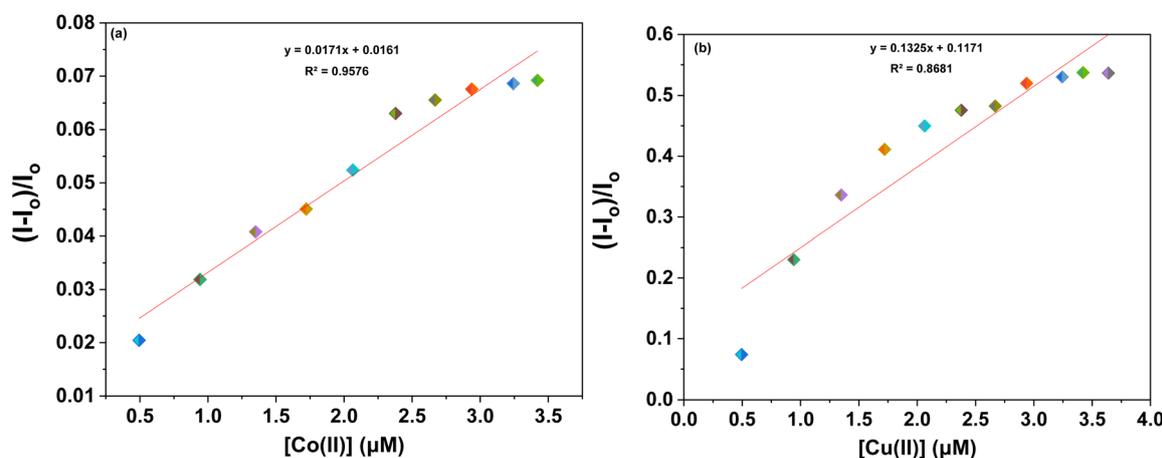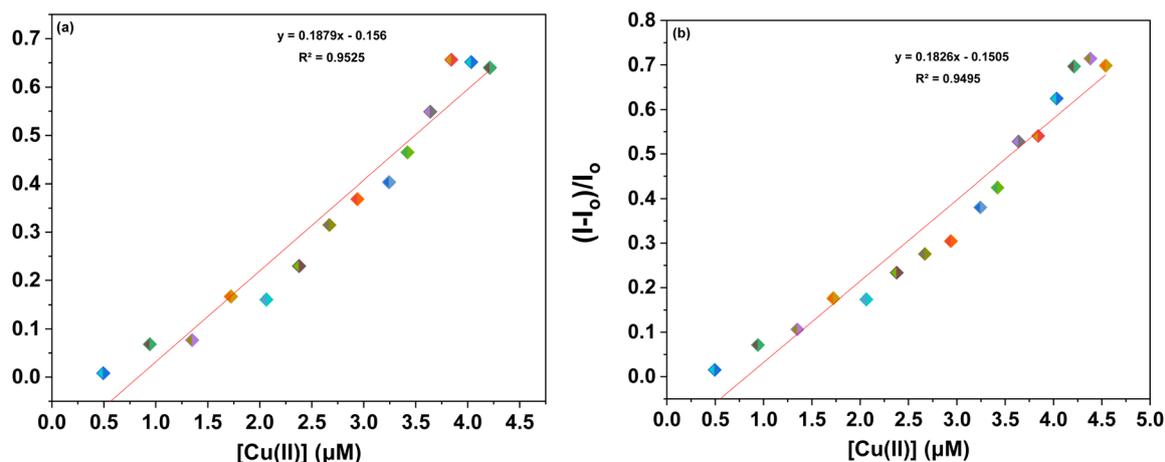

Fig. 7 Correlation plot of probe **6a** illustrating $(I - I_o)/I_o$ *vs.* (a) [Co(II)] and (b) [Cu(II)].

Table 1 LoD, LoQ, association constant, and stoichiometry of probes **6a–6c** on interaction with the respective metal ion

Probe	Metal ion	LoD (μM)	LoQ (μM)	Association constant (K_a) (M^{-1})	Stoichiometry
Probe **6a**	Co(II)	1.64	5.46	8.80×10^3	1 1
	Cu(II)	3.19	10.64	5.99×10^3	
Probe **6b**	Co(II)	2.08	6.94	7.66×10^3	
	Cu(II)	2.30	7.68	4.74×10^3	
Probe **6c**	Co(II)	1.81	6.04	6.61×10^3	
	Cu(II)	1.17	3.92	1.00×10^4	

Fig. 8 Correlation plot of probe **6b** illustrating $(I - I_o)/I_o$ vs. (a) [Co(II)] and (b) [Cu(II)].

to an excitation wavelength (λ_{ex}) of 360 nm, a pronounced emission peak (λ_{em}) at 438 nm was observed. The fluorescence emission intensity of probe **6c** for both Co(II) and Cu(II) (Fig. 6a and b) increased with the addition of metal ions to the solution. The probe concentration was also maintained at 5 μM, while the metal ion concentration was incrementally increased up to 15 equivalents.

Furthermore, to evaluate the sensitivity of the probes towards Co(II) and Cu(II) ions, correlation plots (Fig. 7a, b–9a and b) were used to calculate the limits of detection (LoD) and

quantification (LoQ). The LoD values for probes **6a–6c** for detecting Co(II) were determined to be 1.64 μM, 2.08 μM, and 1.81 μM, respectively, while for detecting Cu(II) ions, the LoD values were 3.19 μM, 2.30 μM, 1.17 μM respectively. The LoQ values for the probes **6a–6c** for the recognition of Co(II) ions were found to be 5.46 μM, 6.94 μM, and 6.04 μM respectively, whereas for Cu(II) ions, the values were 10.64 μM, 7.68 μM, and 3.92 μM respectively are highlighted in the Table 1.

The complexation behavior of probe **6a** with Co(II) and Cu(II) ions was investigated using mass spectrometric analysis (LC-
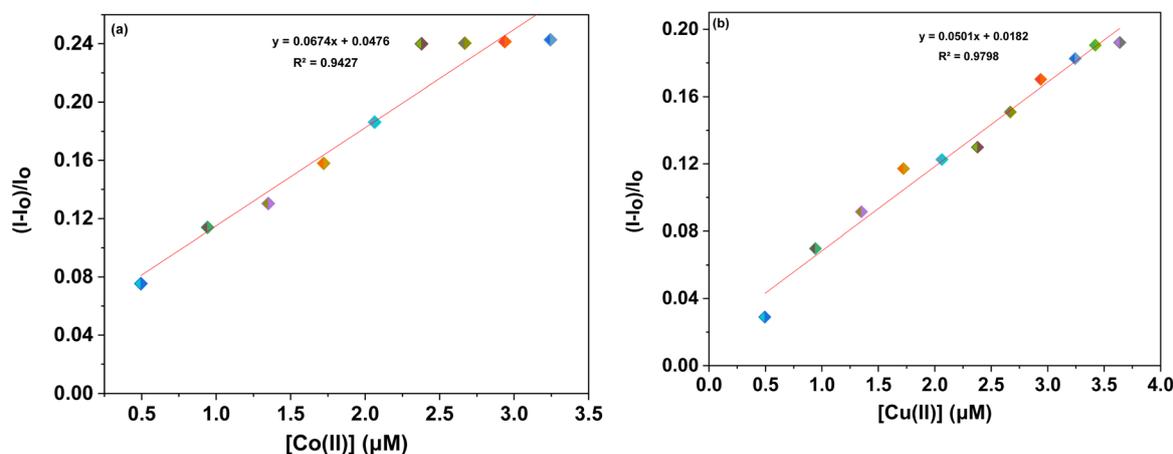

Fig. 9 Correlation plot of probe **6c** illustrating $(I - I_o)/I_o$ vs. (a) [Co(II)] and (b) [Cu(II)].

Table 2 Comparison of 1,2,3-triazole based sensors with the previously reported sensors for the detection of Co(II) and Cu(II)
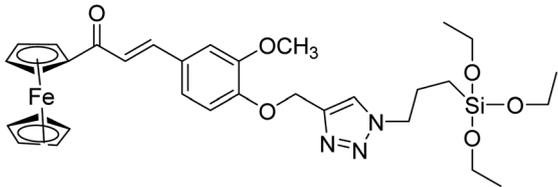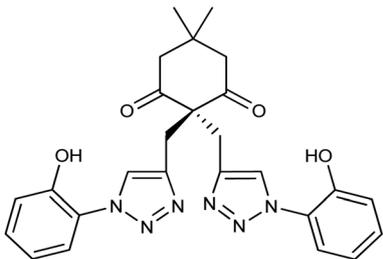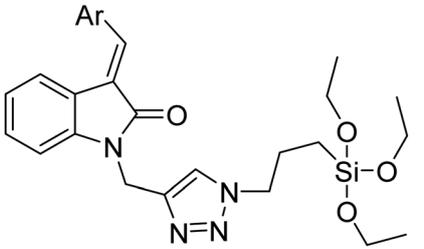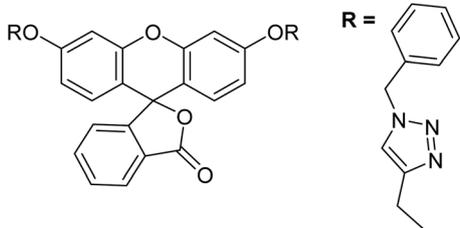
Entry	Structure	Metal ion	LoD (μM)	Reference
1		Cu(II)	9.42	31
2		Cu(II)	2.00	32
3		Cu(II)	3.21	33
4		Co(II)	10.0	5
5		Co(II)	0.012	34
6		Co(II)	1.64	This work
		Cu(II)	3.19	

Table 2 (*Contd.*)

Entry	Structure	Metal ion	LoD (μM)	Reference
7		Co(II) Cu(II)	2.08 2.30	This work
8		Co(II) Cu(II)	1.81 1.17	This work

MS), which confirmed the formation of metal–ligand complexes. Notably, probes **6b** and **6c**, being positional isomers of **6a**, exhibited similar binding stoichiometry and cavity size, indicating analogous coordination behavior. The mass spectrum of the **6a**-Cu(II) and **6a**-Co(II) complexes displayed prominent peaks at *m/z* 734.27 and 731.27, which correspond to the [Cu(II)-probe **6a**-(H$_2$O)$_4$] and [Co(II)-probe **6a**-(H$_2$O)$_4$] species, respectively, as shown in Fig. S58 and S60 (ESI†). Additionally, IR spectral analysis of the metal–ligand complexes revealed the presence of broad peaks at 3355 cm^{-1} and 3351 cm^{-1}, as shown in Fig. S59 and S61† which are attributed to O–H stretching vibrations, suggesting the involvement of coordinated water molecules in the complex.

These findings substantiate the formation of stable coordination complexes with both Cu^{2+} and Co^{2+} ions. Furthermore, density functional theory (DFT) calculations supported the experimental observations by revealing favourable coordination between the metal centers and the nitrogen atoms of the two 1,2,3-triazole moieties within the probe framework, as discussed in detail in the subsequent section (Table 2).

4. Computational analysis

4.1. Structure optimization *via* density functional theory (DFT)

To gain insights into the orbital distribution and energy minimized structures and binding approach of probes **6(a–c)**, comprehensive density functional theory (DFT) calculations using the Gaussian software package.[35] The energy minimized structures of the probe **6a–c** were determined by employing the B3LYP/631 G+(d,p) level of theory (Fig. 10) (cartesian coordinates are provided in the ESI†). However, to investigate the complexation of probes **6a–c** with the Cu(II) and Co(II), the B3LYP/LANL2DZ level of theory was applied. The optimized structures of probes **6a–c** and their complexes are presented in Fig. 11, revealing that one of the nitrogen atoms in each of the 1,2,3-triazole moieties participates in binding the metal ion to the probes.

4.2. Frontier molecular orbitals scrutiny

The chemical behavior of the compounds is primarily influenced by the interaction and overlap between the highest
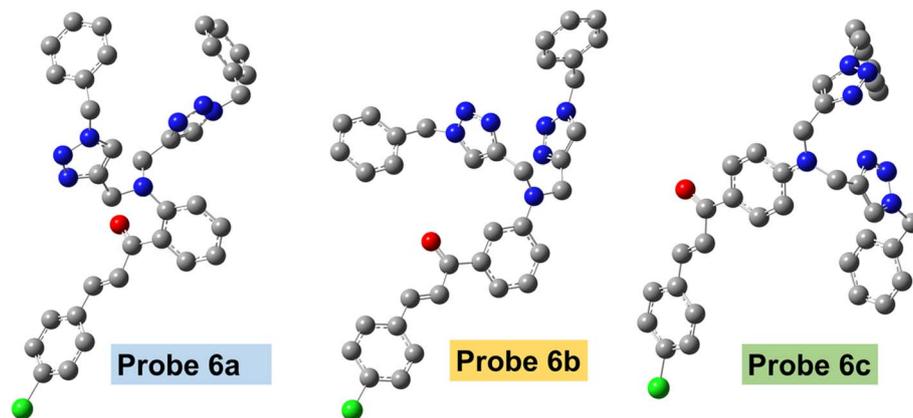
Fig. 10 Energy-minimized structure of probes **6a–6c** through DFT using B3LYP/631 G+(d,p) basis set of theory, respectively (H-atoms have been removed for clarity).

occupied molecular orbital (HOMO) and lowest unoccupied molecular orbital (LUMO), are the key concepts in frontier molecular orbital (FMO) theory used to explain the molecular structures and reactions. The HOMO–LUMO analysis reveals distinct delocalization patterns for probes **6a–6c** and their metal complexes are shown in Fig. 12. DFT calculations revealed that the HOMO–LUMO gap of the free probes **6a**, **6b**, and **6c** were 3.23 eV, 3.11 eV, and 3.40 eV, respectively. Upon coordination
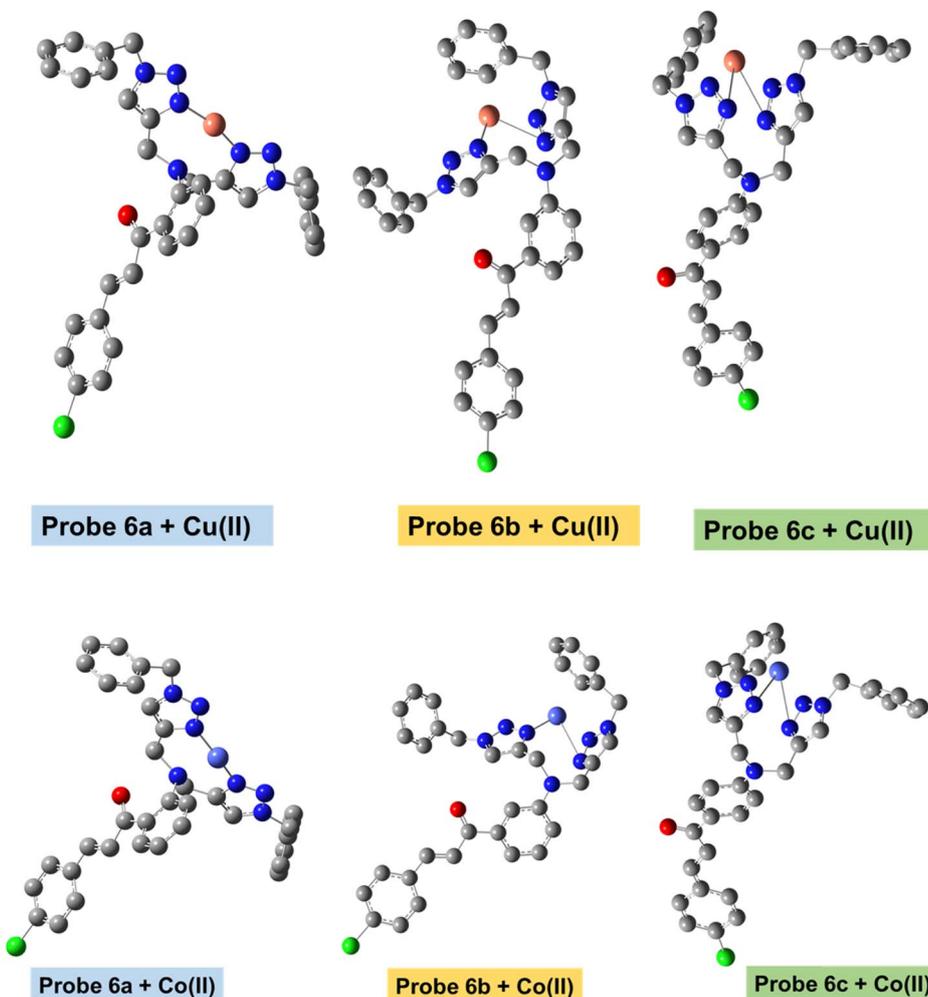

Fig. 11 Energy-minimized structure of probes **6a–6c** with their Co(II) and Cu(II) complexes through DFT using B3LYP/LANL2DZ basis set of theory.
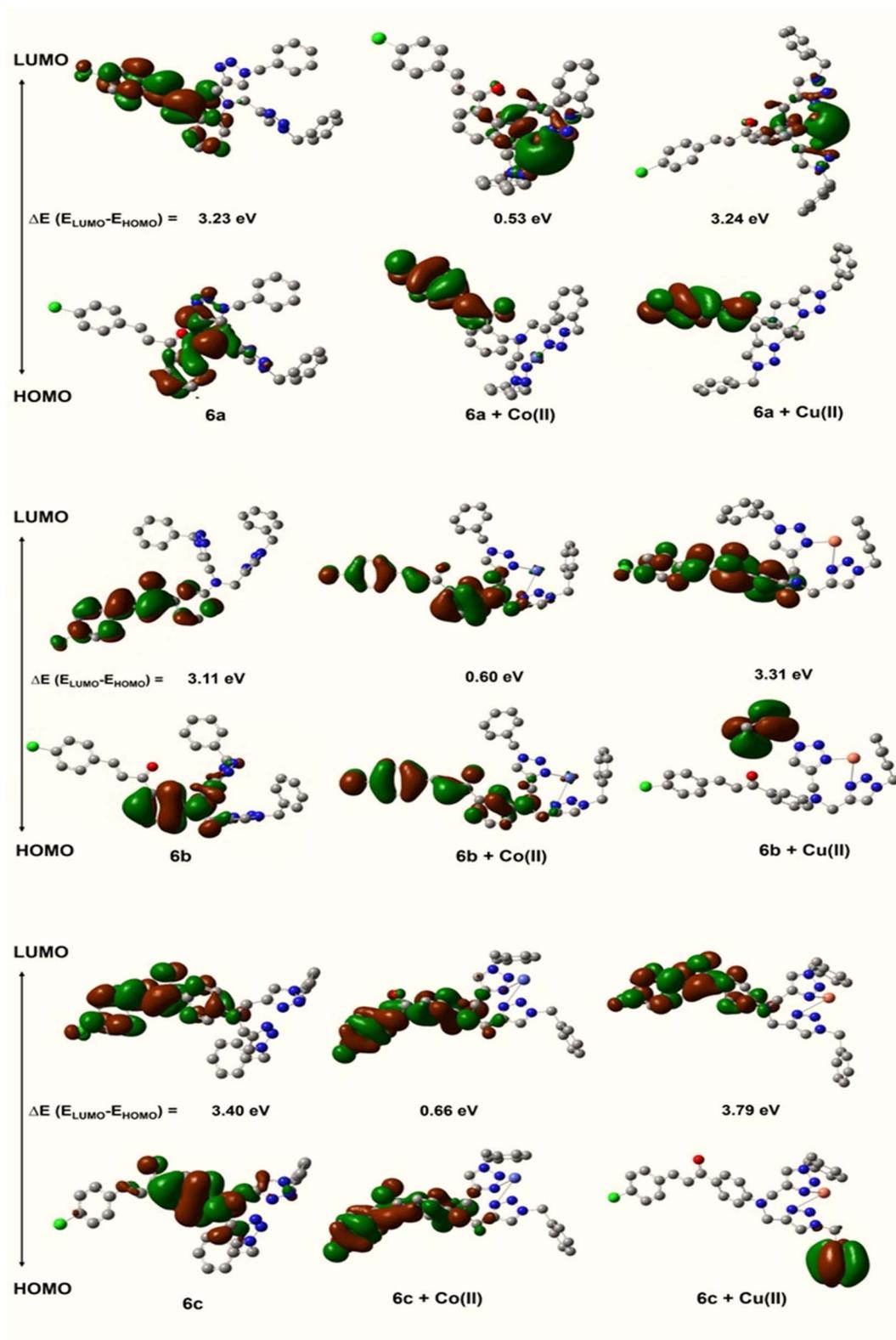
Fig. 12 Density plot depicting the HOMO–LUMO interaction between probes and their respective metal ions.

with Co^{2+} ions, the energy gaps increased slightly to 0.53 eV (**6a**–Co(II)), 0.60 eV (**6b**–Co(II)), and 0.66 eV (**6c**–Co(II)), whereas with Cu^{2+} ions, significantly higher values were observed: 3.24 eV

(**6a**–Cu(II)), 3.31 eV (**6b**–Cu(II)), and 3.79 eV (**6c**–Cu(II)). For probe **6a**, the HOMO is predominantly delocalized over the 1,2,3-triazole moieties, whereas the LUMO is confined to the aromatic
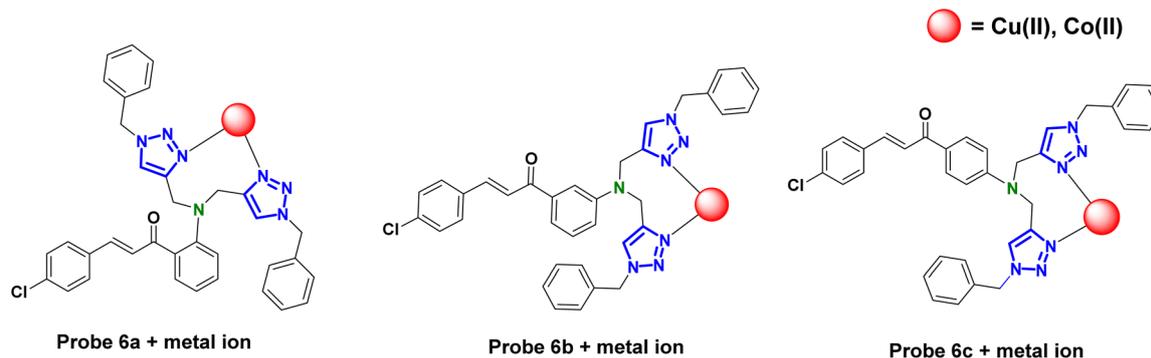
Fig. 13 Plausible mechanism of interaction between probes **6a–c** and their corresponding metal ions.

rings of the chalcone core. Upon coordination with Co(II) and Cu(II) ions, the HOMO shifts to being localized on the aromatic rings of the chalcone backbone, while the LUMO transitions to delocalization over the 1,2,3-triazole moieties. Similarly, the density plots for probe **6b** and its metal complexes, demonstrate that the HOMO is largely delocalized across the 1,2,3-triazole moieties and the chalcone backbone, excluding the terminal aromatic ring, while the LUMO remains localized on the aromatic rings of the parent chalcone structure. For probe **6c**, the HOMO is primarily delocalized over the 1,2,3-triazole moieties and one aromatic ring of the chalcone scaffold, while the LUMO persists in delocalization over the aromatic rings of the chalcone core. These observations highlight the electronic variations induced by metal coordination and structural differences among the probes.

5. Plausible binding mode

Based on Hard-Soft Acid-Base (HSAB) theory,[36] the synthesized probes efficiently capture electron-deficient metal ions through interactions with the lone pair-bearing nitrogen atoms in the 1,2,3-triazole moieties. Both metal ions are known to prefer nitrogen-donor ligands and form stable complexes with N-rich heterocycles. The 1,2,3 triazole ring, containing electron-dense nitrogen atoms at the 2 and 3 positions, serves as an effective coordination site, particularly suited for the borderline Lewis acidic nature of Cu(II) and Co(II). Furthermore, host–guest interactions play a crucial role in sensor design, where a receptor is covalently or coordinately linked to a fluorophore, creating a suitably sized cavity for the incoming metal ion. Upon complexation with the target metal ion, these interactions trigger noticeable changes in the emission intensity. Additionally, DFT calculations reveal that these metal ions form more stable complexes, as indicated by shorter M–N bond lengths and more negative binding energies, revealing that Cu(II) and Co(II) ions preferentially coordinate with the nitrogen atoms of the 1,2,3-triazole groups. The 1,2,3-triazole unit, a key structural feature of probes **6a–6c**, serves as an effective receptor for incoming metal ions due to its nitrogen-rich environment. The Job's plot analysis confirms the formation of 1 : 1 metal–ligand complexes, indicating a strong and selective binding

interaction. The proposed binding mechanism for these interactions is illustrated in Fig. 13.

6. Conclusion

In this study, chalcone-stitched bis-1,2,3-triazole chemosensors (**6a–6c**) were successfully synthesized *via* the CuAAC reaction and explored as selective and sensitive probes for the detection of Cu(II) and Co(II) ions. Their photophysical properties, investigated through UV-vis absorption and fluorescence spectroscopy, demonstrated high selectivity and strong binding affinity toward these toxic metal ions. The probes exhibited time- and temperature-invariant behavior, indicating stable metal–ligand interactions. The Benesi–Hildebrand (B–H) plot analysis confirmed a superior binding affinity for Co(II), a result further corroborated by competitive metal ion titration studies, which established the probes' ability to detect Co(II) ions even in the presence of competing metal ions. Furthermore, DFT calculations provided valuable insights into the molecular configuration and electronic properties of **6a–c**, reinforcing the experimental findings. The strong and stable interactions between the probes and metal ions highlight their potential as efficient and reliable chemosensors. Given their high selectivity, sensitivity, and robust performance, these probes hold significant promise for practical applications in environmental monitoring, water quality assessment, and analytical chemistry. Future studies could focus on broadening the scope of metal ion detection, exploring potential real-world applications, and enhancing probe design for improved sensing capabilities.

Data availability

Data will be made available on request.

Author contributions

Riddima Singh: writing – original draft, investigation, formal analysis. Gurleen Singh: data curation, methodology, resources. Nancy George: data curation, methodology. Gurjaspreet Singh: visualization, validation. Pallavi Markan: formal analysis, resources. Harminder Singh: conceptualization, validation.

Gurpreet Kaur: investigation, writing – review & editing, supervision. Jandeep Singh: conceptualization, supervision.

Conflicts of interest

Authors have no conflicts to declare.

References

1 N. Bereli, D. Cimen, H. Yavuz and A. Denizli, *Sensors for the Detection of Heavy Metal Contaminants in Water and Environment*, Springer, Cham, 2021, vol. 60, pp. 1–21, DOI: **10.1007/978-3-030-63245-8_1**.

2 J. Briffa, E. Sinagra and R. Blundell, Heavy Metal Pollution in the Environment and Their Toxicological Effects on Humans, *Heliyon*, 2020, **6**(9), e04691, DOI: **10.1016/j.heliyon.2020.e04691**.

3 G. Singh, S. Gupta, J. D. Kaur, P. Markan, Vikas, R. Yadav, R. Sehgal, J. Singh and R. Singh, Highly Selective Schiff Base Functionalized Silatrane Based Receptor as Sn(II) Ion Chemosensor: Synthesis, Photophysical, DFT and Docking Studies, *J. Mol. Struct.*, 2023, **1288**, 135687, DOI: **10.1016/j.molstruc.2023.135687**.

4 H. M. Abd El-Lateef, M. M. Khalaf, M. Kandeel and Abdou, A Synthesis, Characterization, DFT, Biological and Molecular Docking of Mixed Ligand Complexes of Ni(II), Co(II), and Cu(II) Based on Ciprofloxacin and 2-(1H-Benzimidazol-2-Yl) Phenol, *Inorg. Chem. Commun.*, 2023, **155**, 111087, DOI: **10.1016/j.inoche.2023.111087**.

5 P. Kaur, B. Lal, N. Kaur, G. Singh, A. Singh, G. Kaur and J. Singh, Selective Two Way Cd(II) and Co(II) Ions Detection by 1,2,3–Triazole Linked Fluorescein Derivative, *J. Photochem. Photobiol. Chem.*, 2019, **382**, 111847, DOI: **10.1016/j.jphotochem.2019.05.010**.

6 P. Saini, G. Singh, G. Singh, J. D. Kaur, G. Kaur, H. Singh and J. Singh, 1-Naphtholphthalein Appended 1,2,3-Triazole *via* CuAAC: A Molecular Assembly for Selective Co(II) Ion Recognition, *Inorg. Chim. Acta*, 2023, **551**, 121470, DOI: **10.1016/j.ica.2023.121470**.

7 J. Sun, X. Xu, G. Yu, W. Li and J. Shi, Coumarin-Based Tripodal Chemosensor for Selective Detection of Cu(II) Ion and Resultant Complex as Anion Probe through a Cu(II) Displacement Approach, *Tetrahedron*, 2018, **74**(9), 987–991, DOI: **10.1016/j.tet.2018.01.013**.

8 A. Ganguly, S. Ghosh, S. Kar and N. Guchhait, Selective Fluorescence Sensing of Cu(II) and Zn(II) Using a Simple Schiff Base Ligand: Naked Eye Detection and Elucidation of Photoinduced Electron Transfer (PET) Mechanism, *Spectrochim. Acta, Part A*, 2015, **143**, 72–80, DOI: **10.1016/j.saa.2015.02.013**.

9 Z. Shabbir, A. Sardar, A. Shabbir, G. Abbas, S. Shamshad, S. Khalid, Natasha, G. Murtaza, C. Dumat and M. Shahid, Copper Uptake, Essentiality, Toxicity, Detoxification and Risk Assessment in Soil-Plant Environment, *Chemosphere*, 2020, **259**, 127436, DOI: **10.1016/j.chemosphere.2020.127436**.

10 D. Luo, X. Wang and W. Feng, Comprehensive Analysis of Cuproptosis and Copper Homeostasis Genotyping and Related Immune Land Scape in Lung Adenocarcinoma, *Sci. Rep.*, 2023, **13**(1), 16554, DOI: **10.1038/s41598-023-43795-3**.

11 T. Litwin, A. Antos, J. Bembenek, A. Przybyłkowski, I. Kurkowska-Jastrzębska, M. Skowrońska and A. Członkowska, Copper Deficiency as Wilson's Disease Overtreatment: A Systematic Review, *Diagnostics*, 2023, **13**(14), 2424, DOI: **10.3390/diagnostics13142424**.

12 Z. Zhu, M. Song, J. Ren, L. Liang, G. Mao and M. Chen, Copper Homeostasis and Cuproptosis in Central Nervous System Diseases, *Cell Death Dis.*, 2024, **15**(11), 1–15, DOI: **10.1038/s41419-024-07206-3**.

13 S. Dutta, S. Let, M. M. Shirolkar, A. V. Desai, P. Samanta, S. Fajal, Y. D. More and S. K. Ghosh, A Luminescent Cationic MOF for Bimodal Recognition of Chromium and Arsenic Based Oxo-Anions in Water, *Dalton Trans.*, 2021, **50**(29), 10133–10141, DOI: **10.1039/D1DT01097B**.

14 Y. Li, Y. Du, Y. Zhou, Q. Chen, Z. Luo, Y. Ren, X. Chen and G. Chen, Iron and Copper: Critical Executioners of Ferroptosis, Cuproptosis and Other Forms of Cell Death, *Cell Commun. Signal.*, 2023, **21**(1), 327, DOI: **10.1186/s12964-023-01267-1**.

15 X. Chen, Q. Cai, R. Liang, D. Zhang, X. Liu, M. Zhang, Y. Xiong, M. Xu, Q. Liu, P. Li, P. Yu and A. Shi, Copper Homeostasis and Copper-Induced Cell Death in the Pathogenesis of Cardiovascular Disease and Therapeutic Strategies, *Cell Death Dis.*, 2023, **14**(2), 1–12, DOI: **10.1038/s41419-023-05639-w**.

16 L. Chen, Q. Lin, D. Yuan and Z. Gong, Simultaneous Measurement of Trace Levels of Hg, As, Sb, and Bi in Coastal Seawater with a Multichannel Chemical Vapor Generation Atomic Fluorescence Spectrometer, *Anal. Chem.*, 2023, **95**(42), 15621–15627, DOI: **10.1021/acs.analchem.3c02755**.

17 H. Liu, Q. Meng, X. Zhao, Y. Ye and H. Tong, Inductively Coupled Plasma Mass Spectrometry (ICP-MS) and Inductively Coupled Plasma Optical Emission Spectrometer (ICP-OES)-Based Discrimination for the Authentication of Tea, *Food Control*, 2021, **123**, 107735, DOI: **10.1016/j.foodcont.2020.107735**.

18 A. Nourbakhsh, M. Rahimnejad, M. Asghary and H. Younesi, Simultaneous Electro-Determination of Trace Copper, Lead, and Cadmium in Tap Water by Using Silver Nanoparticles and Graphene Nanoplates as Nanocomposite Modified Graphite Electrode, *Microchem. J.*, 2022, **175**, 107137, DOI: **10.1016/j.microc.2021.107137**.

19 S. Dutta, A. Sinelshchikova, J. Andreo and S. Wuttke, Nanoscience and Nanotechnology for Water Remediation: An Earnest Hope toward Sustainability, *Nanoscale Horiz.*, 2024, **9**(6), 885–899, DOI: **10.1039/D4NH00056K**.

20 T. O. Hara and B. Singh, Electrochemical Biosensors for Detection of Pesticides and Heavy Metal Toxicants in Water: Recent Trends and Progress, *ACS EST Water*, 2021, **1**(3), 462–478, DOI: **10.1021/acsestwater.0c00125**.

21 F. Qian, R. Jia, M. Cheng, A. Chaudhary, S. Melhi, S. D. Mekkey, N. Zhu, C. Wang, F. Razak, X. Xu, C. Yan,

X. Bao, Q. Jiang, J. Wang and M. Hu, An Overview of Polylactic Acid (PLA) Nanocomposites for Sensors, *Advances in Composite Hybrid Mater*, 2024, **7**(3), 75, DOI: **10.1007/s42114-024-00887-6**.

22 N. An, T. Chen, J. Zhang, G. Wang, M. Yan and S. Yang, Rational Electrochemical Design of Cuprous Oxide Hierarchical Microarchitectures and Their Derivatives for SERS Sensing Applications, *Small Methods*, 2024, **8**(5), 2300910, DOI: **10.1002/smtd.202300910**.

23 S. Dutta, S. Fajal and S. K. Ghosh, Heavy Metal-Based Toxic Oxo-Pollutants Sequestration by Advanced Functional Porous Materials for Safe Drinking Water, *Acc. Chem. Res.*, 2024, **57**(17), 2546–2560, DOI: **10.1021/acs.accounts.4c00348**.

24 X. Fu, Z. Niu, C. Peng, H. Han, W. Sun and T. Yue, Quantitative Synergistic Adsorption Affinity of Ca(II) and Sodium Oleate to Predict the Surface Reactivity of Hematite and Quartz, *Sep. Purif. Technol.*, 2025, **360**, 131196, DOI: **10.1016/j.seppur.2024.131196**.

25 Z. Esmaeeli, M. R. Khodabakhshi, Z. Mirjafary and H. Saeidian, Efficient Synthesis of Novel 1, 2, 3-Triazole-Based Diazepam Derivatives by Click CuAAC Reaction: Spectroscopic Characterizations and DFT Studies, *J. Mol. Struct.*, 2021, **1246**, 131206, DOI: **10.1016/j.molstruc.2021.131206**.

26 M. Meldal and F. Diness, Recent Fascinating Aspects of the CuAAC Click Reaction, *THEOCHEM*, 2020, **2**(6), 569–584, DOI: **10.1016/j.trechm.2020.03.007**.

27 F. Ahmed and H. Xiong, Recent Developments in 1,2,3-Triazole-Based Chemosensors, *Dyes Pigm.*, 2021, **185**, 108905, DOI: **10.1016/j.dyepig.2020.108905**.

28 R. Singh, G. Singh, N. George, G. Singh, A. Dalal, H. Singh, G. Kaur and J. Singh, Chalcone-Ensembled 1,2,3-Triazole *via* Click Chemistry: Selective 'Turn-On' Detection of Cu(II) Ions *via* Photoinduced Electron Transfer in Real Water Samples and Computational Analysis, *J. Mol. Struct.*, 2025, **1325**, 140921, DOI: **10.1016/j.molstruc.2024.140921**.

29 S. Sharma, S. Dutta, G. K. Dam and S. K. Ghosh, Neutral Nitrogen Donor Ligand-Based MOFs for Sensing Applications, *Chem.–Asian J.*, 2021, **16**(18), 2569–2587, DOI: **10.1002/asia.202100638**.

30 J. Kozłowska, B. Potaniec, D. Baczyńska, B. Żarowska and M. Anioł, Synthesis and Biological Evaluation of Novel Aminochalcones as Potential Anticancer and Antimicrobial Agents, *Molecules*, 2019, **24**(22), 4129, DOI: **10.3390/molecules24224129**.

31 G. Singh, A. Arora, S. Rani, P. Kalra and M. Kumar, A Click-Generated Triethoxysilane Tethered Ferrocene-Chalcone-Triazole Triad for Selective and Colorimetric Detection of Cu^{2+} Ions, *ChemistrySelect*, 2017, **2**(13), 3637–3647, DOI: **10.1002/slct.201700186**.

32 D. Ghosh, S. Rhodes, D. Winder, A. Atkinson, J. Gibson, W. Ming, C. Padgett, S. Landge and K. Aiken, Spectroscopic Investigation of Bis-Appended 1,2,3-Triazole Probe for the Detection of Cu(II) Ion, *J. Mol. Struct.*, 2017, **1134**, 638–648, DOI: **10.1016/j.molstruc.2016.12.096**.

33 G. Singh, P. Kalra, A. Arora, A. Singh, G. Sharma, S. Sanchita and P. Satija, Chalcone Scaffolds as Photofunctional Hybrid Material of Indolin-2-One-Functionalized Siloxy Framework for Optical Sensing of Cu^{2+}, *New J. Chem.*, 2018, **42**(20), 16902–16910, DOI: **10.1039/C8NJ02884B**.

34 G. Singh, S. Devi, A. Singh, P. Satija, Tamana, Heena, T. Diskit, A. Dalal and B. Mohan, A Click-Generated Chalcone Allied Triazole Sensor for Co (II) with INHIBIT Logic Gate Construction and Its Antioxidant Properties, *Spectrochim. Acta, Part A*, 2025, **328**, 125450, DOI: **10.1016/j.saa.2024.125450**.

35 M. J. Frisch, G. W. Trucks, H. B. Schlegel, G. E. Scuseria, M. A. Robb, J. R. Cheeseman, G. Scalmani, V. Barone, B. Mennucci, G. A. Petersson, H. Nakatsuji, M. Caricato, X. Li, H. P. Hratchian, A. F. Izmaylov, J. Bloino, G. Zheng, J. L. Sonnenberg, M. Hada, M. Ehara, K. Toyota, R. Fukuda, J. Hasegawa, M. Ishida, T. Nakajima, Y. Honda, O. Kitao, H. Nakai, T. Vreven, J. A. Montgomery Jr, J. E. Peralta, F. Ogliaro, M. Bearpark, J. J. Heyd, E. Brothers, K. N. Kudin, V. N. Staroverov, R. Kobayashi, J. Normand, K. Raghavachari, A. Rendell, J. C. Burant, S. S. Iyengar, J. Tomasi, M. Cossi, N. Rega, J. M. Millam, M. Klene, J. E. Knox, J. B. Cross, V. Bakken, C. Adamo, J. Jaramillo, R. Gomperts, R. E. Stratmann, O. Yazyev, A. J. Austin, R. Cammi, C. Pomelli, J. W. Ochterski, R. L. Martin, K. Morokuma, V. G. Zakrzewski, G. A. Voth, P. Salvador, J. J. Dannenberg, S. Dapprich, A. D. Daniels, O. Farkas, J. B. Foresman, J. V. Ortiz, J. Cioslowski and D. J. Fox, *Gaussian 09, Revision B.01*, Gaussian Inc., 2010, Wallingford.

36 R. G. Pearson, Hard and Soft Acids and Bases, *J. Am. Chem. Soc.*, 1963, **85**(22), 3533–3539, DOI: **10.1021/ja00905a001**.